A Journal of the Gesellschaft Deutscher Chemiker

Angewandte International Edition GDCh Chemie

www.angewandte.org

## Accepted Article

**Title:** Fabrication of Highly Oriented Ultrathin Zr-MOF Membrane from Nanosheets towards Unprecedented Gas Separation

**Authors:** Yanwei Sun, Jiahui Yan, Yunlei Gao, Taotao Ji, Sixing Chen, Chen Wang, Peng Lu, Yanshuo Li, and Yi Liu



**To be cited as:** *Angew. Chem. Int. Ed.* **2023**, e202216697

**Link to VoR:** https://doi.org/10.1002/anie.202216697

WILEY-VCH

10.1002/anie.202216697

RESEARCH ARTICLE

WILEY-VCH

# Fabrication of Highly Oriented Ultrathin Zirconium Metal-Organic Framework Membrane from Nanosheets towards Unprecedented Gas Separation

Yanwei Sun,[a] Jiahui Yan,[a] Yunlei Gao,[a] Taotao Ji,[a] Sixing Chen,[a] Chen Wang,[a] Peng Lu,[b] Yanshuo Li,[b] and Yi Liu*[a, b, c]

[a] Dr. Y. Sun, J. Yan, Y. Gao, T. Ji, S. Chen, C. Wang, Prof. Dr. Y. Liu
State Key Laboratory of Fine Chemicals, Frontiers Science Center for Smart Materials, School of Chemical Engineering
Dalian University of Technology
Dalian 116024, China
E-mail: diligenliu@dlut.edu.cn

[b] Prof. Dr. Y. Li, Prof. Dr. P. Lu
School of Materials Science and Chemical Engineering
Ningbo University
Ningbo, 315211 China

[c] Prof. Dr. Y. Liu
Dalian Key Laboratory of Membrane Materials and Membrane Processes
Dalian University of Technology
Dalian 116024, China

Supporting information for this article is given via a link at the end of the document.

**Abstract:** Concurrent regulation of crystallographic orientation and membrane thickness of zirconium metal-organic framework (Zr-MOF) membranes is challenging but promising for their performance enhancement. In this study, we pioneered the fabrication of uniform triangular-shaped, 40 nm thick UiO-66 nanosheet (NS) seeds by employing an anisotropic etching strategy. Through innovating confined counter-diffusion-assisted epitaxial growth, highly (111)-oriented 165 nm-thick UiO-66 membrane was prepared. The significant reduction in thickness and diffusion barrier in the framework endowed the membrane with unprecedented $CO_2$ permeance (2070 GPU) as well as high $CO_2/N_2$ selectivity (35.4), which surpassed the performance limits of state-of-the-art polycrystalline MOF membranes. In addition, highly (111)-oriented 180 nm-thick $NH_2$-UiO-66 membrane showing superb $H_2/CO_2$ separation performance with $H_2$ permeance of 1230 GPU and $H_2/CO_2$ selectivity of 41.3, was prepared with the above synthetic procedure.

## Introduction

Membrane-based separation has shown great potential for gas separation in view of energy efficiency and small carbon footprints.[1] Recent decades witnessed considerable attention paid to metal-organic framework (MOF) membranes due to their high porosity, excellent thermal stability, tunable framework structure, and rich functionality.[2] Nevertheless, their separation performances are still suffered from the permeability-selectivity trade-off. It has been proven that the microstructure (like orientation, thickness, and grain boundary structure) of MOF membranes exerted a significant influence on their separation performances.[3] Ideally, highly oriented ultrathin MOF membranes are desirable for transcending their performance upper bound. Among various methods, epitaxial growth has proven to be capable of precisely controlling the microstructure of MOF membranes due to an effective decoupling of nucleation and growth processes.[4] Nevertheless, the following obstacles must be overcome for preparing highly oriented ultrathin MOF (in particular, 3D MOF) membranes: First, facile preparation of

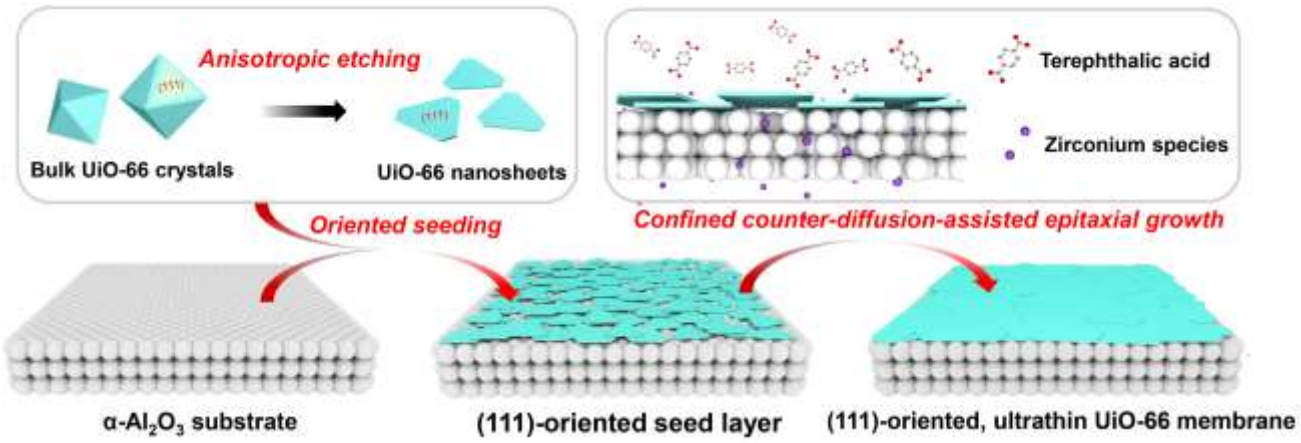


**Figure 1.** The procedure for the preparation of highly (111)-oriented ultrathin UiO-66 membrane.

uniform MOF nanosheet (NS) seeds. Although great achievements have been made in the synthesis of MOF NSs, the applicability of the methods developed so far is mainly restricted to 2D MOF materials; in contrast, recent progress made in preparing 3D MOF NSs remained quite limited. In addition, it is equally important to inhibit excessive growth in the vertical direction with no compromise in membrane continuity. Although several approaches have been developed to modulate the epitaxial growth of oriented MOF membranes in the lateral direction relative to the vertical direction, how to minimize the growth rate in the vertical direction with no compromise in continuity remains largely unexplored to date. Third, suppression of twin growth during epitaxial growth, since twin generation may lead to increased intercrystalline defects and therefore, inferior gas separation performance.

UiO-66, a prototypical member of Zr-MOFs with 3D topology, represents a promising candidate for membrane-based $CO_2$ separation due to appropriate pore size, high affinity for $CO_2$, and exceptional chemical stability.[5] We recently found that maintaining preferred (111)-orientation was beneficial for enhancing $CO_2/N_2$ separation performances of UiO-66 membranes.[6] A significant reduction in membrane thickness has become indispensable to improving their separation performances further.

However, currently using octahedral-shaped UiO-66 seeds (≥ 400 nm in size) represents the only option for preparing highly (111)-oriented UiO-66 membranes. As a result, the thickness of the obtained UiO-66 membrane is limited by that of the seed layer, which hinders further enhancement of the $CO_2$ permeance. To overcome the above obstacles, developing a facile strategy for synthesizing UiO-66 NS seeds with ultrathin thickness (≤50 nm) has become indispensable. Nevertheless, their preparation remains elusive to date, although tremendous efforts have been devoted to the morphology and size regulation of UiO-66 crystals.[7,8]

In recent decades, anisotropic etching has proven quite effective in preparing hollow-structured MOF crystals through the preferential dissolution of their bulk counterparts along specific facets.[9] For instance, Maspoch et al. synthesized uniform hollow ZIF-8 crystals via xylenol orange etching through selective breaking coordination bonds between $Zn^{2+}$ ions and 2-mIm ligands.[9a] Recently, Yu et al. demonstrated that $WO_4^{2-}$ anions could react with $[Zr_6O_4(OH)_4]$ cluster nodes in the UiO-66 framework via neutralization reaction, resulting in the formation of uniform bipyramid-shaped hollow UiO-66 crystals through etching their bulk counterparts.[9e] Motivated by these achievements, herein we speculate that triangular ultrathin UiO-66 NSs may be obtained through further prolonging the etching duration, which, however, still deserves further verification.

In this study, we fabricated highly (111)-oriented 165 nm-thick UiO-66 membrane through innovating NS seed preparation and epitaxial growth processes, which were briefly described as follow (**Figure 1**): Initially, a novel progressive anisotropic etching strategy was employed for preparing uniform triangular-shaped 40 nm-thick UiO-66 NSs. Subsequently, oriented UiO-66 seed layer supported on the porous α-$Al_2O_3$ disk was obtained via spin-coating technique. Finally, highly (111)-oriented 165 nm-thick UiO-66 membrane was prepared via confined counter-diffusion-based epitaxial growth. To the best of our knowledge, this represented the first report of the preparation of sub-200-nm-thick oriented 3D MOF membranes. Among various influencing factors, preparation of uniform UiO-66 NS seeds via anisotropic etching, the conduction of confined counter-diffusion-assisted epitaxial growth, and using $ZrS_2$ as metal precursor during epitaxial growth cooperatively contributed to the formation of UiO-66 membranes with optimized microstructure. Gas permeation results indicated that the $CO_2/N_2$ separation performance of prepared UiO-66 membrane was the highest among pristine pure MOF membranes measured under comparable conditions. In the same manner, we prepared highly (111)-oriented 180 nm-thick $NH_2$-UiO-66 membrane showing superb $H_2/CO_2$ separation performance, thus confirming its generality for separation performance enhancement of MOF membranes.

## Results and Discussion

The first step involved the preparation of UiO-66 NS seeds. In this study, we explored the preparation of uniform UiO-66 NS seeds via precise anisotropic etching of bulk UiO-66 crystals (denoted as P-UiO-$66_{RT}$) synthesized by a simple solvothermal method at room temperature. As shown in Figure 2a, obtained bulk UiO-66 crystals were octahedral-shaped with an average size of 800 nm. After wet-chemical etching in an $Na_2WO_4$ solution under controlled conditions, uniform triangle-shaped UiO-66 NSs with side length of ~600 nm could be obtained (Figure 2b, c). Relevant AFM image (Figure 2d) indicated that the thickness of UiO-66 NSs was ~40 nm. TEM results further confirmed that there existed substantial mesopores inside UiO-66 NSs (Figure 2e). Crystal phase and crystallinity of the prepared NSs were convinced by the relevant XRD pattern, which exhibited a characteristic peak assigned to the (111) plane of UiO-66 (Figure 2f). While a significant loss of crystallinity of the obtained UiO-66 NSs could be attributed to severe structural degradation during the etching process. In addition, the appearance of a broad hump with 2θ value in the range of 15-35° was indicative of the presence of amorphous phase, which commonly possessed higher chemical activity than its crystalline counterpart due to the abundant provision of unsaturated coordination sites and dangling bonds.[10] Relevant FT-IR spectra revealed identical characteristic vibrations as their bulk counterparts (Figure S1), thus confirming that the coordination interaction between $[Zr_6O_4(OH)_4]$ cluster nodes and terephthalic acid ($H_2BDC$) ligands was largely preserved after anisotropic etching.

Simultaneously, textural properties of UiO-66 NSs were studied through the analysis of their $N_2$ sorption isotherms (77 K) featuring a steep uptake at $P/P_0$=0-0.02 and a hysteresis loop at $P/P_0$=0.45-1.0, which was indicative of the presence of hierarchical pore structure (Figure 2g). The BET surface area of UiO-66 NSs was calculated to be 357 $m^2\ g^{-1}$, which was lower than that of P-UiO-$66_{RT}$ (1010 $m^2\ g^{-1}$) due to partial collapse of the framework. The micropore size distribution of UiO-66 NSs was the same as P-UiO-$66_{RT}$ (0.68 nm), while the BJH pore size distribution of UiO-66 NSs further revealed the presence of mesopores centering at 3.7 and 14.4 nm (Figure S2), which was consistent with the above TEM observation. Given the potential impact of gas adsorption capacity and selectivity on the $CO_2/N_2$ separation performance, $CO_2$ and $N_2$ adsorption isotherms of UiO-66 NSs were further measured at RT. As shown in Figure 2h, compared with P-UiO-$66_{RT}$, UiO-66 NSs exhibited a certain reduction in $CO_2$ and $N_2$ adsorption capacity; nevertheless, the $CO_2/N_2$ IAST selectivity (36.4) (Figure 2i, Table

S1) at relatively high pressure remained unchanged, which was beneficial for maintaining high $CO_2/N_2$ selectivity of the corresponding UiO-66 membranes. It was worth mentioning that, UiO-66 NSs showed a reverse trend in IAST selectivity. This could be attributed to the existence of abundant unsaturated $Zr^{4+}$ originating from the lower crystallinity, which not only promoted stronger quadrupolar interactions with $CO_2$, but also restricted $N_2$ diffusion into the pores, thus leading to increased IAST selectivity with increasing pressure. To verify the preferential binding affinity of UiO-66 framework towards $CO_2$, isosteric adsorption heat ($Q_{st}$) values of $CO_2$ and $N_2$ on UiO-66 NSs and P-UiO-$66_{RT}$ were calculated from the temperature-dependent isotherms at 273 and 298 K using the Clausius-Clapeyron equation (Figure S3). It was observed that both UiO-66 NSs and P-UiO-$66_{RT}$ possessed higher $Q_{st}$ values for $CO_2$ than $N_2$ at lower adsorption amount, indicating that both UiO-66 NSs and P-UiO-$66_{RT}$ exhibited preferential binding affinity towards $CO_2$. While the gradual reduction of $Q_{st}$ value with increasing adsorption amount was a sign of the existence of $CO_2$-selective binding sites either.

To gain insights into the mechanism of UiO-66 NS formation, morphological evolution of bulk UiO-66 crystals during the process of anisotropic etching was studied (Figure 3). At the early stage, edges and vertices of bulk UiO-66 crystals were more vulnerable to nucleophilic attack by etching agents (i.e., $WO_4^{2-}$ anions); in counterst, relevant facets parallel to the (111) plane remained intact (Figure 3a). After etching for 2 h, the interior of UiO-66 crystals was largely dissolved, thus forming a hollow-shaped structure as confirmed by relevant TEM image (Figure 3b). Further prolonging the etching duration to 3 h resulted in progressive thinning in all directions, therefore forming hollow-shaped UiO-66 crystals with completely dissolved vertices and partially segregated edges (Figure 3c). Finally, uniform triangular-shaped UiO-66 NSs were obtained due to complete edge etching (Figure 2b). The mechanism of etching-induced UiO-66 NS formation was schematically illustrated in Figure 3d. Of particular note, the reason why the etching preferentially occurred at vertices and edges can be

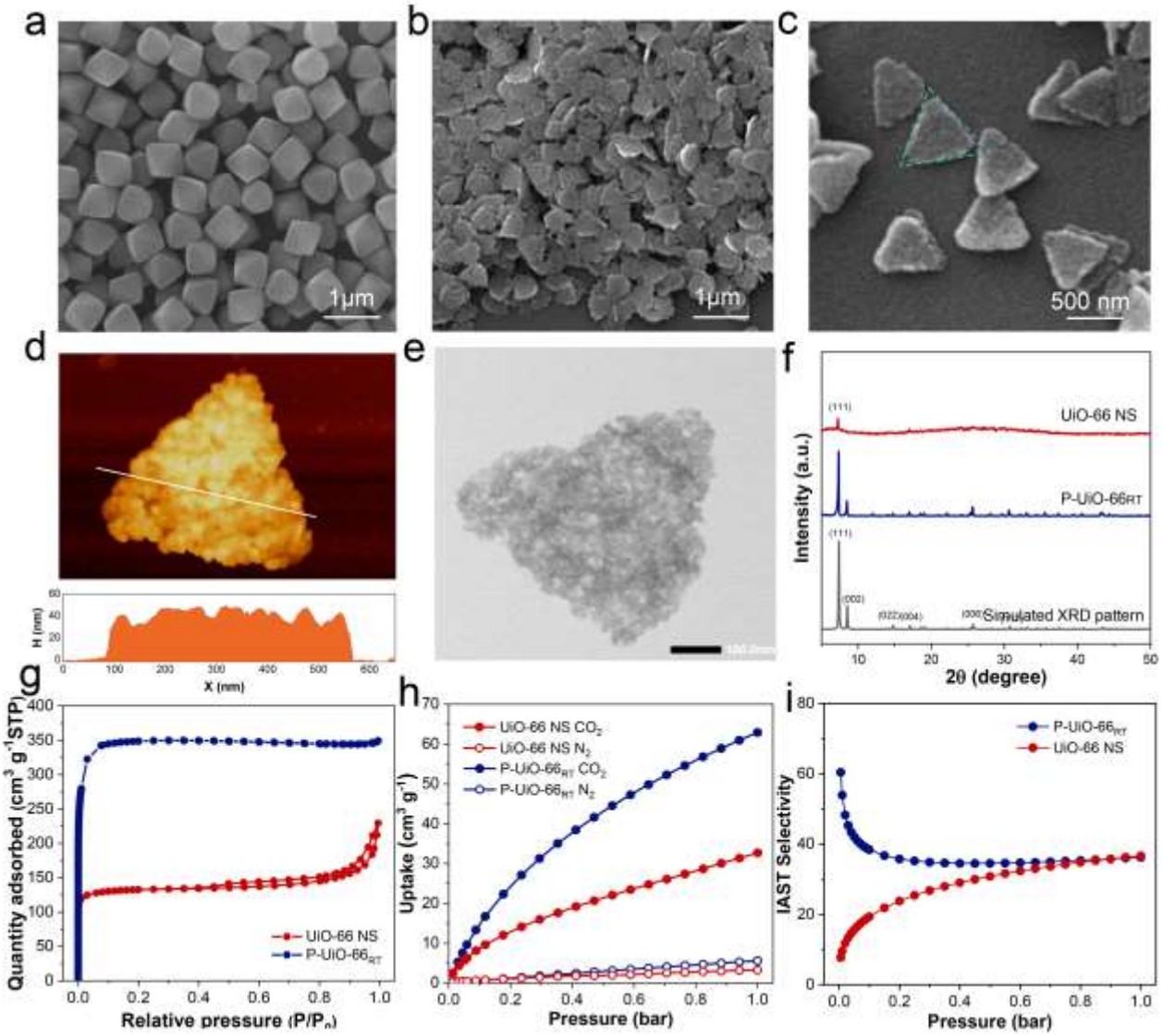


**Figure 2** Characterization of bulk UiO-66 crystals (denoted as P-UiO-$66_{RT}$) synthesized at room temperature and UiO-66 nanosheets (NSs) prepared via anisotropic etching. (a) SEM images of P-UiO-$66_{RT}$. (b, c) SEM images, (d) AFM image, and (e) TEM image of UiO-66 NSs. (f) XRD patterns, (g) $N_2$ sorption isotherm, (h) $CO_2$ and $N_2$ adsorption isotherms, and (i) $CO_2/N_2$ IAST selectivity of P-UiO-$66_{RT}$ and UiO-66 NSs.

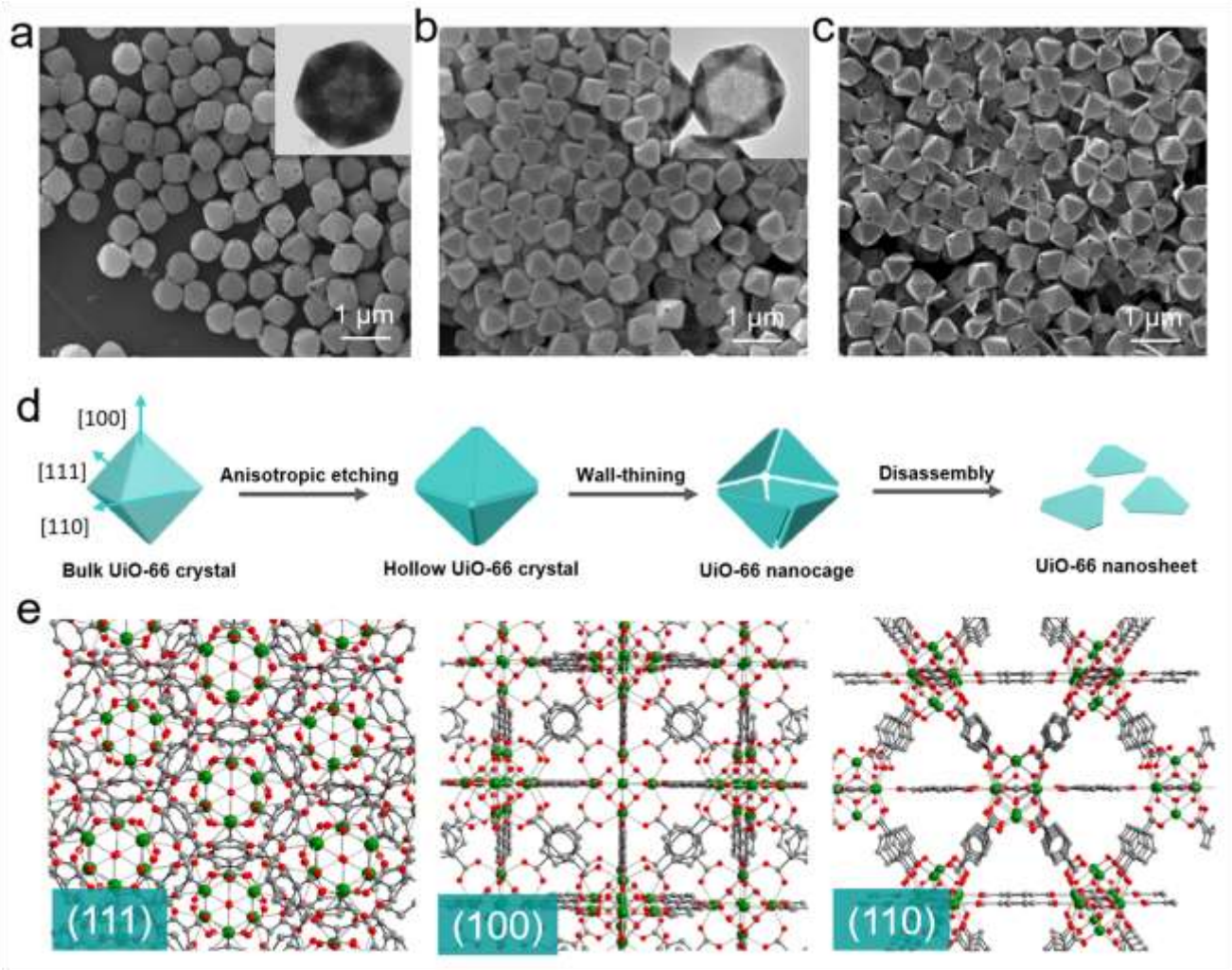


**Figure 3** SEM and TEM images of UiO-66 prepared by anisotropic etching for (a) 1 h, (b) 2 h, and (c) 3 h. (d) Schematic diagram of the formation process of UiO-66 NSs. (e) Schematic illustration of the crystal structure of UiO-66 along different directions. Zr, C, and O atoms are represented as green, grey, and red spheres, respectively.

attributed to a higher surface Gibbs free energy there. In addition, as illustrated by the framework topology of UiO-66 (Figure 3e), (110) and (100) facets possess lower atomic packing density and larger pore openings in comparison with that of the (111) facet, which implies that the former can be more easily accessed by $WO_4^{2-}$ anions, resulting in preferential etching of bulk UiO-66 crystals along [100] and [110] lattice directions.[9a, b]

It is noteworthy that the use of bulk UiO-66 crystals synthesized at RT was the prerequisite for obtaining uniform triangular-shaped UiO-66 NSs. For comparison, bulk UiO-66 crystals synthesized at 120 °C. (denoted as P-UiO-$66_{120}$) were subjected to anisotropic etching following the same procedure as described above. Our results indicated that only cracked nanocages and trace amounts of UiO-66 NSs could be obtained after etching (Figure S4). The morphological discrepancy could be ascribed to different missing-linker numbers in the UiO-66 framework. To be specific, missing-linker numbers in the framework of P-UiO-$66_{120}$ and P-UiO-$66_{RT}$, as confirmed by the calculation results based on the method developed by Lillerud,[11] were 0.80 and 1.44, respectively (Figure S5). Obviously, more defective P-UiO-$66_{RT}$ were more susceptible to nucleophilic attack by $WO_4^{2-}$ anions, rendering it easier to ensure complete etching of edges and vertices; simultaneously, larger pore size of P-UiO-$66_{RT}$ (0.68 nm) in comparison with that of P-UiO-$66_{120}$ (0.61 nm) was advantageous for faster diffusion of $WO_4^{2-}$ anions in the framework, making it more efficient for etching the interior of bulk UiO-66 crystals (Figure S6).

Our research indicated that etching temperature exerted crucial influence on final appearance of etched UiO-66 crystals. UiO-66 NSs could not be obtained at etching temperatures lower than 180 °C (Figure S7); in addition, we found that carrying out etching reaction under static heating condition instead of dynamic heating condition led to the formation of non-uniform UiO-66 crystals due to the difficulty in eliminating temperature and concentration gradients in the reaction vessel (Figure S8).

Subsequently, the obtained UiO-66 NSs were uniformly deposited on the porous α-$Al_2O_3$ substrate via spin-coating technique. SEM images indicated that the seed layer was uniform, closely packed, and 120 nm-thick (shown in Figure 4a and S9). In addition, only the (111) reflection located at 2θ value of 6.7° was observed in the XRD pattern (shown in Figure 4f), thus confirming that the seed layer was highly (111) oriented.

In the next step, epitaxial growth was performed to fill remaining intergranular gaps in the seed layer. Initially, $ZrCl_4$ was used as metal source. Nevertheless, its high reactivity resulted in explosive bulk nucleation and therefore, severe crystal twinning in the UiO-66 membrane (Figure S10). Our previous study indicated that using 2D transition metal sulfides (e.g., $ZrS_2$) as metal source enabled effective bulk nucleation inhibition and

twin suppression during epitaxial growth.[12] Therefore, $ZrS_2$ was used as zirconium source in this study. SEM images showed that a well-intergrown and smooth UiO-66 membrane could be obtained after epitaxial growth, confirming that undesired crystal twinning had been effectively suppressed; nevertheless, its thickness sharply increased to ~700 nm, which could be attributed to the existence of large open space on top of the seed layer, resulting in excessive growth in the vertical direction (Figure S11). It is therefore anticipated that an innovative approach enabling the suppression of epitaxial growth in the vertical direction with no compromise in membrane continuity could be developed.

The counter-diffusion synthetic protocol, referring to physical segregation of two precursor solutions containing metal ions and organic ligands with porous supports followed by their concentration-gradient-driven assembly, has shown promising opportunities for ultrathin MOF membrane preparation due to its "self-regulating" ability to terminate MOF crystal growth upon forming a continuous MOF layer.[13] Wang pioneered the preparation of continuous ZIF-8 membranes via counter-diffusion method.[14] In this study, a confined counter-diffusion approach was further developed to achieve epitaxial growth of highly (111)-oriented ultrathin UiO-66 membrane. To be specific, trace amounts of $ZrS_2$, which served as sole metal source, were deposited on the back side of the seed layer-deposited porous α-$Al_2O_3$ substrate, followed by epitaxial growth in a ligand-containing precursor solution (Figure S12).

As shown in Figure 4c, after epitaxial growth, a well-intergrown 165 nm-thick UiO-66 membrane showing flat surface morphology was obtained (Figure 4d). The corresponding EDXS mapping showed a sharp transition between the UiO-66 layer and underlying substrate (Figure 4e), implying that the UiO-66 crystals did not penetrate deep in the substrate pores; simultaneously, only a diffraction peak assigned to the (111) plane could be discerned in the XRD pattern (Figure 4f), thus confirming that prepared UiO-66 membrane was highly (111)-oriented. As far as we know, this represented the thinnest oriented 3D MOF membrane as reported in literatures.[4,15]

In addition, we found that the membrane thickness was only slightly increased compared with the seed layer, confirming that employing confined counter-diffusion significantly inhibited the epitaxial growth in the vertical direction. Subsequently, the relative lateral growth rate ($v_r = v_{lateral}/v_{vertical}$) of epitaxial growth layer was calculated. Our results indicated that $v_r$ of the above UiO-66 membrane reached 8.9, which was much higher than that of the UiO-66 membrane prepared by conventional epitaxial growth ($V_r$=1.1) (Table S2).

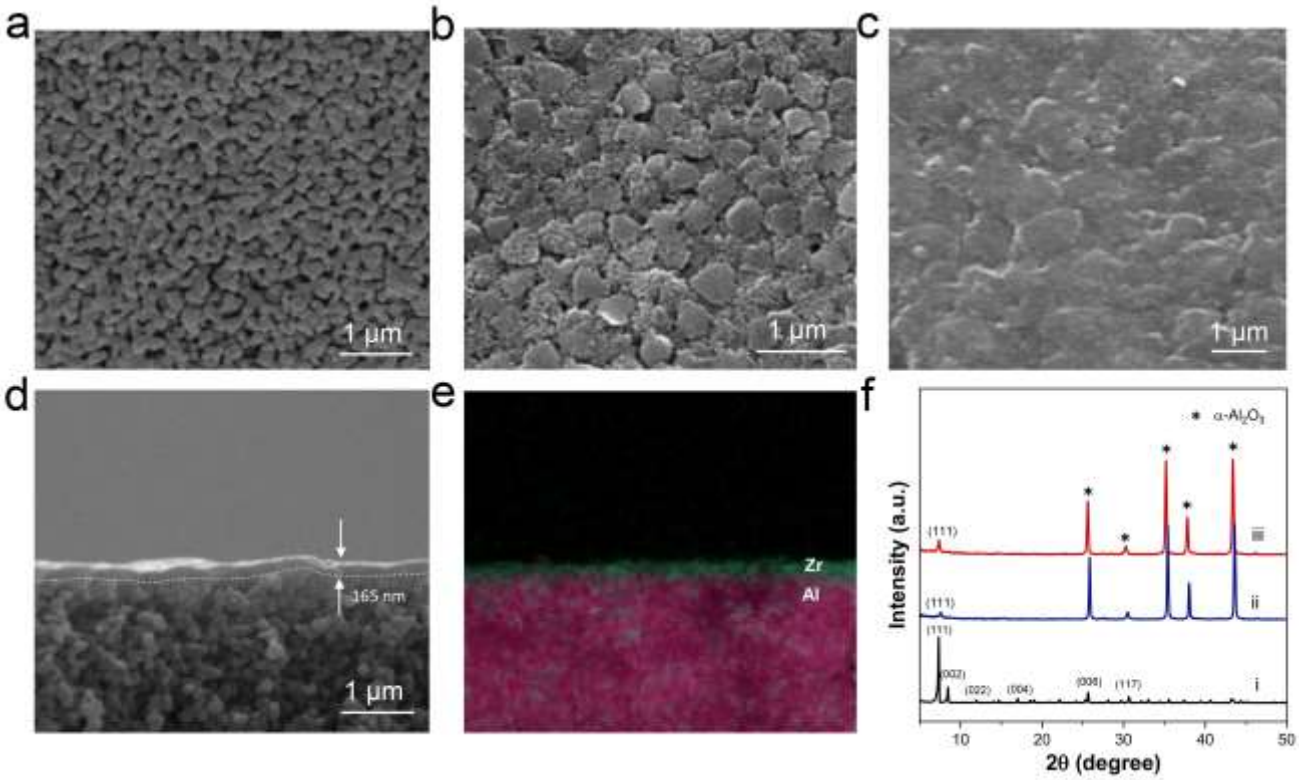


**Figure 4** SEM images of (a) porous α-$Al_2O_3$ substrate, (b) UiO-66 NS seed layer, and (c, d) UiO-66 membrane prepared by confined counter-diffusion epitxial growth at 150 °C for 6 h. (e) EDXS mapping of Zr (color code: green) and Al (color code: pink) distributions at the cross-section of prepared UiO-66 membrane. (f) XRD patterns of (i) simulated XRD pattern, (ii) (111)-oriented seed layer, and (iii) (111)-oriented UiO-66 membrane.

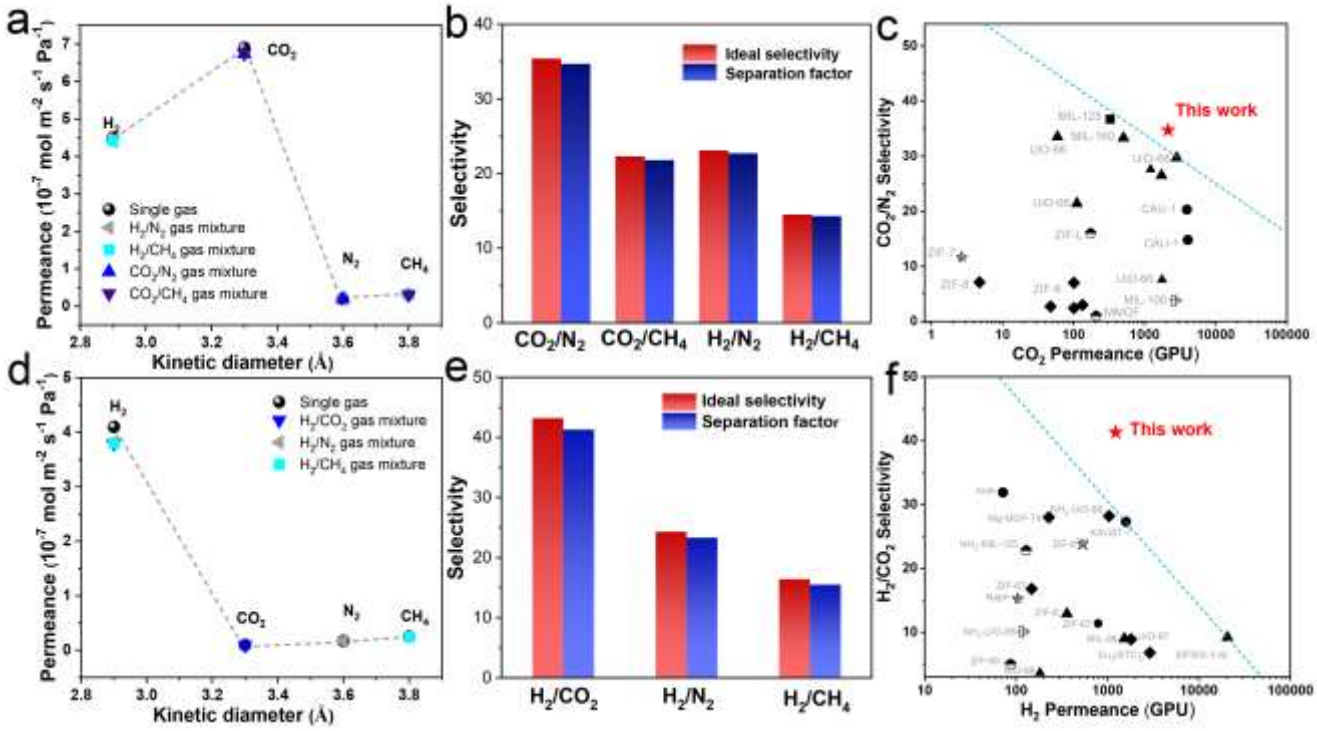


**Figure 5** (a) Single and mixed gas permeances of the UiO-66 membrane measured under ambient conditions. (b) Ideal selectivity and separation factor of different gas pairs through the UiO-66 membrane. (c) Comparison of the $CO_2/N_2$ separation performance of the UiO-66 membrane with other pristine polycrystalline MOF membranes measured under similar conditions. (d) Single and mixed gas permeances of the $NH_2$-UiO-66 membrane measured under ambient conditions. (e) Ideal selectivity and separation factor of different gas pairs through the $NH_2$-UiO-66 membrane. (f) Comparison of the $H_2/CO_2$ separation performance of the $NH_2$-UiO-66 with other pristine polycrystalline 3D MOF membranes measured under similar conditions. Detailed data were listed in Table S3–S6.

The significant reduction in epitaxial growth rate in the vertical direction could be ascribed to concentration gradients hindering the diffusion of nutrients in the seed layer. Compared with conventional epitaxial growth, effective segregation of $H_2$BDC ligand-containing solution and $ZrS_2$ source with the porous substrate led to the generation of concentration gradients of $H_2$BDC ligands and dissolved Zr species at the substrate-solution interface. Furthermore, narrow and tortuous intergranular spaces in the seed layer played decisive roles in modulating the relative lateral epitaxial growth rate: On the one hand, owing to a sufficient supply of nutrients (i.e., both Zr species and BDC ligands) within intergranular spaces, relatively high epitaxial growth rate in the lateral direction could be guaranteed; on the other hand, owing to large concentration gradients of dissolved Zr species, their concentration on top of the seed layer was fairly low, thus leading to kinetically limited epitaxial growth in the vertical direction. In addition, our results showed that pre-deposition of the oriented seed layer, which provided not only a confined space for counter-diffusion but also heterogeneous nucleation sites for epitaxial growth, was indispensable for the formation of highly (111)-oriented ultrathin UiO-66 membrane. As shown in the comparative experiment, direct employment of bare porous α-$Al_2O_3$ substrate would lead to the formation of a discontinuous and randomly oriented UiO-66 layer even under optimized synthetic conditions (Figure S13).

It is expected that our UiO-66 membrane will show enhanced $CO_2/N_2$ separation performance due to a multi-scale microstructural superiority, i.e., high missing-linker number (1.44), preferred-(111) orientation, and ultrathin thickness (165 nm). Finally, single gas and binary gas mixture permeation tests were performed using the Wicke-Kallenbach technique (Figure S14). Our results showed that the permeance of $CO_2$ ($6.9\times10^{-7}$ mol m$^{-2}$ s$^{-1}$ Pa$^{-1}$) was the highest compared with other gas molecules; moreover, the $CO_2/N_2$, $CO_2/CH_4$, $H_2/N_2$ and $H_2/CH_4$ selectivity of prepared UiO-66 membrane, which reached 35.4, 22.7, 23.1 and 14.5, was far beyond the corresponding Knudsen selectivity, thus confirming that there existed few grain boundary defects in the membrane (Figure 5a, Table S3). To determine the origin of the high $H_2/N_2$ and $H_2/CH_4$ selectivity, adsorption and diffusion coefficients of different gases in UiO-66 membranes were further calculated according to the membrane permeability and gas sorption isotherms at room temperature (Figure S15). It was observed that the $H_2$ diffusion coefficient was much higher than that of $CH_4$ and $N_2$, while the adsorption coefficient of $H_2$ was lower than that of $CH_4$ and $N_2$, thus proving that the high $H_2/N_2$ and $H_2/CH_4$ selectivity was mainly attributed to the high $H_2/N_2$ and $H_2/CH_4$ diffusion selectivity.[16] In effect, many literatures have reported the preparation of larger pore-sized membranes with high $H_2/N_2$ or $H_2/CH_4$ selectivity. It was therefore possible that the unique framework topology of UiO-66 contributed to the decent $H_2/N_2$ and $H_2/CH_4$ separations. Moreover, the preferred (111)-orientation was beneficial for reducing grain boundary defects and therefore, enhancing the $H_2/N_2$ and $H_2/CH_4$ selectivity further. Of particular note, its $CO_2/N_2$ separation performance easily transcended the upper bound of state-of-the-art MOF membranes tested under similar conditions (Figure 5c, Table S4). In addition, the online stability test indicated that both $CO_2$ permeance and separation factor (SF) of equimolar $CO_2/N_2$ gas mixture were kept unchanged within 20 h (Figure S16), thus indicating an excellent operation stability.

To verify the generality of this approach, we further prepared highly (111)-oriented 180 nm-thick $NH_2$-UiO-66 membrane (Figure S17) following identical synthetic procedure except that $NH_2$-BDC ligands were used instead. Gas permeation results (Figure 5e, Table S5) indicated that the ideal $H_2/CO_2$ selectivity

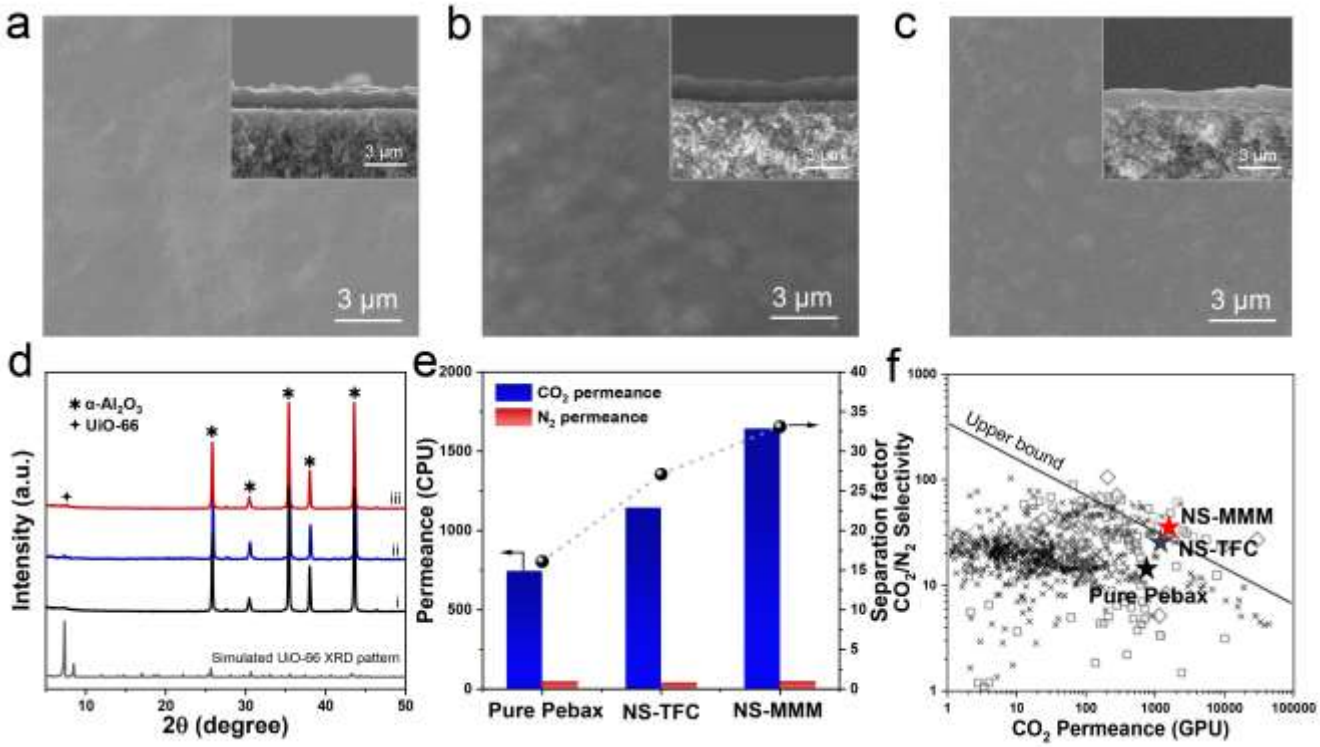


**Figure 6.** (a-c) SEM images of prepared pure Pebax 2533 membrane, UiO-66 NS-loaded mixed-matrix membrane ,and thin film composite membrane using UiO-66 NS gutter layer (denoted as Pure Pebax, NS-MMM and NS-TFC, respectively), and (d) corresponding XRD patterns of (i) Pure Pebax, (ii) NS-MMM and (iii) NS-TFC. (e) $CO_2/N_2$ separation performance of different membranes. (f) Comparison $CO_2/N_2$ separation performances of prepared composite membranes with 2008 Robeson upper bound.[17]

reached 43.4, which was superior to all other $NH_2$-UiO-66 membranes (Figure 5d). Adsorption and diffusion coefficients of gas molecules in the prepared $NH_2$-UiO-66 membrane were further calculated according to the membrane permeability and gas adsorption isotherms (Figure S18). It was observed that compared with $CO_2$, $H_2$ showed the highest diffusion coefficient (ca. $10^{-6}$ $cm^2$ $s^{-1}$) in the $NH_2$-UiO-66 framework, implying that fast diffusion of $H_2$ in the membrane contributed to the high $H_2$ permeance; simultaneously, $NH_2$-UiO-66 only exhibited a negligible $H_2$ uptake (0.79 $cm^3$ $g^{-1}$) compared with $CO_2$ (59.6 $cm^3$ $g^{-1}$), thus confirming a weak interaction between the $NH_2$-UiO-66 framework and $H_2$. In contrast, the diffusion coefficient of $CO_2$ in the $NH_2$-UiO-66 framework was significantly reduced from $10^{-8}$ (in the UiO-66 framework) to $10^{-10}$ $cm^2$ $s^{-1}$; simultaneously, $Q_{st}$ value of $CO_2$ on $NH_2$-UiO-66 (32.4 kJ $mol^{-1}$) was much higher than that on UiO-66 (28.2 kJ $mol^{-1}$), which was indicative of a stronger affinity interaction between $CO_2$ and $NH_2$-UiO-66 framework (Figure S19). The strong interaction in turn inhibited the desorption or motion of $CO_2$ (i.e., random walk jumping frequency and jump length of $CO_2$ were reduced), resulting in a reduction in the $CO_2$ diffusion coefficient. We therefore deduced that the high $H_2/CO_2$ selectivity dominantly originated from the high $H_2/CO_2$ diffusion selectivity, owing to strong interaction between -$NH_2$ functional groups in the $NH_2$-UiO-66 framework and $CO_2$ Moreover, its $H_2/CO_2$ separation performance surpassed the upper bound of state-of-the-art 3D MOF membranes reported in literatures (Figure 5f, Table S6), thus demonstrating the significance of multi-scale microstructural optimization in separation performance enhancement of MOF membranes.

To investigate the potential of UiO-66 NSs in the field of composite membranes, we prepared two kinds of membranes including UiO-66 NS-loaded mixed-matrix membrane (denoted as NS-MMM) and thin film composite membrane using UiO-66 NS gutter layer (denoted as NS-TFC), and their separation performances were systematically investigated and compared with pure Pebax 2533 membrane (denoted as Pure Pebax). As shown in SEM images, all prepared membranes showed smooth top surface and defect-free cross-section under optimized conditions (Figure 6a-c). Corresponding XRD patterns confirmed the existence of UiO-66 NSs in both NS-MMM and NS-TFC (Figure 6d).

As shown in Figure 6e, 4 wt.% NS-MMM exhibited both increased $CO_2/N_2$ separation factor (from 16.1 to 33.1) and $CO_2$ permeance (from 747 to 1650 GPU), which was 105.6% and 86.8% higher than that of Pure Pebax membrane, respectively. The enhanced separation performance could be attributed to the introduction of UiO-66 NSs, which led to both higher free volume of MMM (i.e., higher $CO_2$ permeability) and $CO_2/N_2$ diffusion selectivity (i.e., higher $CO_2/N_2$ selectivity). Considering its potential application in industrial separation of $CO_2$ from flue gas, the effect of feed composition on the separation performance of 4 wt.% NS-MMM was investigated further. Our results indicated that with the increase of the volume fraction of $CO_2$ in the feed side, the $CO_2$ permeability increased slightly as opposed to the decrease of $CO_2/N_2$ SF. In the case of simulated flue gas ($V_{CO2}$:$V_{N2}$=15:85), 4 wt.% NS-MMM displayed higher separation factor (39.3), which was attractive for their practical application (Figure S20a). Moreover, the $CO_2$ permeance could be maintained at a high value (1633 Barrer). As a result, the $CO_2/N_2$ separation performance of 4 wt.% NS-MMM well exceeded the 2008 polymer upper-bound (Figure 6f), indicating the importance of incorporation of UiO-66 NS fillers in improving the $CO_2/N_2$ separation performance of Pebax 2533 membrane.

In addition, our results implied that compared with pure Pebax 2533 membrane, NS-TFC also exhibited superior $CO_2/N_2$ separation factor (27.1) and $CO_2$ permeance (1146 GPU). This could be interpreted by the adsorption competition between two feed gases towards UiO-66 NS gutter layer. The effect of $CO_2$ concentration in the feed side on the separation performance of prepared TFC membrane was investigated further. Being analogous to NS-MMM, both the $CO_2/N_2$ selectivity and $CO_2$ permeance of the NS-TFC increased with increasing $CO_2$ concentration. In the case of simulated flue gas ($V_{CO2}$:$V_{N2}$=15:85), the NS-TFC displayed higher separation factor (31.5), which was attractive for their practical application either (Figure S20b). Based on the above results, we concluded that the prepared UiO-NSs held great potential in the field of MMM and TFC membranes.

## Conclusion

To summarize, in this study we successfully prepared highly (111)-oriented 165 nm-thick UiO-66 membrane through oriented epitaxial growth of the UiO-66 NS seed layer. A novel anisotropic etching approach was developed for the synthesis of uniform triangular-shaped UiO-66 NS seeds, while concurrent use of confined counter-diffusion and $ZrS_2$ source during epitaxial growth was found indispensable for retarding the growth rate in the vertical direction with no compromise in membrane continuity. Owing to a multi-scaled microstructural superiority, the $CO_2/N_2$ separation performance of prepared UiO-66 membrane easily surpassed the upper bound of state-of-the-art MOF membranes measured under similar conditions. Following identical synthetic procedure, highly (111)-oriented 180 nm-thick $NH_2$-UiO-66 membrane exhibiting superior $H_2/CO_2$ separation performance could be prepared either, thus showing great promise for separation performance enhancement of versatile polycrystalline MOF membranes.

## Acknowledgements

We are grateful to National Natural Science Foundation of China (22108025), the Postdoctoral Science Foundation of China (2021TQ0054), National Natural Science Foundation of China (22078039), Science and Technology Innovation Fund of Dalian (2020JJ26GX026), Fok Ying-Tong Education Foundation of China (171063), Science Fund for Creative Research Groups of the National Natural Science Foundation of China (22021005), National Key Research and Development Program of China (2019YFE0119200), and the Fundamental Research Fundamental Funds for the Central Universities (DUT22LAB602) for the financial support.

## Conflict of Interest

The authors declare no conflict of interest.

## Data Availability Statement

Research data are not shared.

**Keywords:** MOF membrane • nanosheets • gas separation • orientation

[1] a) D. S. Sholl, R. P. Lively, *Nature* **2016,** *532*, 435-437; b) R. W. Baker, B. T. Low, *Macromolecules* **2014,** *47*, 6999-7013; c) S. Hong, Y. Jeong, H. Baik, N. Choi, A. C. K. Yip, J. Choi, *Angew. Chem. Int. Ed.* **2021**, *60*, 1323-1331; *Angew. Chem.* **2021**, *133*, 1343-1351.

[2] a) Y. Peng, Y. Li, Y. Ban, H. Jin, W. Jiao, X. Liu, W. Yang, *Science* **2014,** *346*, 1356-1359; b) X. Ma, P. Kumar, N. Mittal, A. Khlyustova, P. Daoutidis, K. A. Mkhoyan, M. Tsapatsis, *Science* **2018,** *361*, 1008-1011; c) A. Knebel, B. Geppert, K. Volgmann, D. I. Kolokolov, A. G. Stepanov, J. Twiefel, P. Heitjans, D. Volkmer, J. Caro, *Science* **2017,** *358*, 347-351; d) X. Wang, Q. Lyu, T. Tong, K. Sun, L.-C. Lin, C. Y. Tang, F. Yang, M. D. Guiver, X. Quan, Y. Dong, *Nat. Commun.* **2022,** *13*, 266; S. Zhou, O. Shekhah, A. Ramírez, P. Lyu, E. Abou-Hamad, J. Jia, J. Li, P. M. Bhatt, Z. Huang, H. Jiang, T. Jin, G. Maurin, J. Gascon, M. Eddaoudi, *Nature* **2022,** *606*, 706-712.

[3] a) Y. Liu, Y. Ban, W. Yang, *Adv. Mater.* **2017,** *29*, 1606949; b) C. Zhang, B.-H. Wu, M.-Q. Ma, Z. Wang, Z.-K. Xu, *Chem. Soc. Rev.* **2019,** *48*, 3811-3841; c) Q. Hou, S. Zhou, Y. Wei, J. Caro, H. Wang, *J. Am. Chem. Soc.* **2020,** *142*, 9582-9586; d) R. Xu, Y. Kang, W. Zhang, X. Zhang, B. Pan, *Angew. Chem. Int. Ed.* **2022,** *61*, e202115443; *Angew. Chem.* **2022**, *134*, e202115443.

[4] a) Y. Yoo, Z. Lai, H.-K. Jeong, *Microp. Mesop. Mater.* **2009,** *123*, 100-106; b) Y. S. Li, H. Bux, A. Feldhoff, G. L. Li, W. S. Yang, J. Caro, *Adv. Mater.* **2010,** *22*, 3322-3326; c) X. Ma, Z. Wan, Y. Li, X. He, J. Caro, A. Huang, *Angew. Chem. Int. Ed.* **2020,** *59*, 20858-20862; *Angew. Chem.* **2020**, *132*, 21044-21048

[5] a) X. Liu, N. K. Demir, Z. Wu, K. Li, *J. Am. Chem. Soc.* **2015,** *137*, 6999-7002; b) M. H. Mohamed, Y. Yang, L. Li, S. Zhang, J. P. Ruffley, A. G. Jarvi, S. Saxena, G. Veser, J. K. Johnson, N. L. Rosi, *J. Am. Chem. Soc.* **2019,** *141*, 13003-13007; c) G. Yu, X. Zou, L. Sun, B. Liu, Z. Wang, P. Zhang, G. Zhu, *Adv. Mater.* **2019,** *31*, 1806853; d) S. Friebe, B. Geppert, F. Steinbach, J. Caro, *ACS Appl. Mater. Interfaces* **2017**, *9*, 12878–12885.

[6] a) J. Yan, Y. Sun, T. Ji, L. Liu, M. Zhang, Y. Liu, *J. Membr. Sci.* **2021,** *635*, 119515; b) J. Yan, Y. Sun, T. Ji, C. Zhang, L. Liu, Y. Liu, *J. Membr. Sci.* **2022,** *653*, 120496.

[7] Y. Wang, W. Zhang, J. Guo, W. Duan, B. Liu, *ACS Appl. Mater. Interfaces* **2019,** *11*, 38016-38022.

[8] Y. Han, M. Liu, K. Li, Y. Zuo, Y. Wei, S. Xu, G. Zhang, C. Song, Z. Zhang, X. Guo, *CrystEngComm* **2015,** *17*, 6434-6440.

[9] a) C. Avci, J. Ariñez‐Soriano, A. Carné‐Sánchez, V. Guillerm, C. Carbonell, I. Imaz, D. Maspoch, *Angew. Chem. Int. Ed.* **2020,** *54,* 14417-14421*; Angew. Chem.* **2020,** *127*, 14625-14629; b) Z. X. Cai, Z. L. Wang, Y. J. Xia, H. Lim, W. Zhou, A. Taniguchi, M. Ohtani, K. Kobiro, T. Fujita, Y. Yamauchi, *Angew. Chem. Int. Ed.* **2021,** *60,* 4747-4755*; Angew. Chem.* **2021,** *133*, 4797-4805; c) Z. Zhang, Y. Tao, H. Tian, Q. Yue, S. Liu, Y. Liu, X. Li, Y. Lu, Z. Sun, E. Kraka, *Chem. Mater.* **2020,** *32*, 5550-5557; d) L. Han, X. Y. Yu, X. W. Lou, *Adv. Mater.* **2016,** *28*, 4601-4605; e) J. Wei, N. Cheng, Z. Liang, Y. Wu, Z. Zou, Z. Zhuang, Y. Yu, *J. Mater. Chem. A* **2018,** *6*, 23336-23344; f) T. Bao, Y. Zou, C. Zhang, C. Yu, C. Liu, *Angew. Chem. Int. Ed.* **2022**, 61, e202209433; *Angew. Chem.* **2022**, 134, e202209433.

[10] a) M. Elmaalouf, M. Odziomek, S. Duran, M. Gayrard, M. Bahri, C. Tard, A. Zitolo, B. Lassalle-Kaiser, J.-Y. Piquemal, O. Ersen, C. Boissière, C. Sanchez, M. Giraud, M. Faustini, J. Peron, *Nat. Commun.* **2021,** *12*, 3935; b) L. Wu, A. Longo, N. Y. Dzade, A. Sharma, M. M. R. M. Hendrix, A. A. Bol, N. H. de Leeuw, E. J. M. Hensen, J. P. Hofmann, *ChemSusChem* **2019,** *12*, 4383-4389; c) Y. Kang, C. Liu, Y. Zhang, H. Xing, M. Jiang, *J Non Cryst Solids* **2018,** *500*, 453-459; d) K. Wei, X. Wang, X. Jiao, C. Li, D. Chen, *Appl. Surf. Sci.* **2021,** *550*, 149323; e) Y. Kamigaki, S. i. Minami, H. Kato, *J. Appl. Phys.* **1990,** *68*, 2211-2215.

[11] G. C. Shearer, S. Chavan, J. Ethiraj, J. G. Vitillo, S. Svelle, U. Olsbye, C. Lamberti, S. Bordiga, K. P. Lillerud, *Chem. Mater.* **2014,** *26*, 4068-4071.

[12] Y. Sun, C. Song, X. Guo, Y. Liu, *ACS Appl. Mater. Interfaces* **2020,** *12*, 4494-4500.

[13] a) K. Huang, Q. Li, G. Liu, J. Shen, K. Guan, W. Jin, *ACS Appl. Mater. Interfaces* **2015,** *7*, 16157-16160; b) N. Wang, X. Li, L. Wang, L. Zhang, G. Zhang, S. Ji, *ACS Appl. Mater. Interfaces* **2016,** *8*, 21979-21983; c) H. T. Kwon, H.-K. Jeong, *J. Am. Chem. Soc.* **2013,** *135*, 10763-10768; d) Y. Sun, H. Huang, X. Guo, Z. Qiao, C. Zhong, *ChemNanoMat* **2019,** *5*, 1244-1250.

[14] J. Yao, D. Dong, D. Li, L. He, G. Xu, H. Wang, *Chem. Commun.* **2011,** *47*, 2559-2561.

[15] a) Y. Sun, Y. Liu, J. Caro, X. Guo, C. Song, Y. Liu, *Angew. Chem. Int. Ed.* **2018**, *57,* 16088-16093; *Angew. Chem.* **2018***, 130,* 16320-16325; b) Y. Liu, G. Zeng, Y. Pan, Z. Lai, *J. Membr. Sci.* **2018**, *379*, 46-51; c) S. Friebe, B. Geppert, F. Steinbach, J. R. Caro, *ACS Appl. Mater. Interfaces* **2017**, *9*, 12878-12885; d) H. Bux, A. Feldhoff, J. Cravillon, M. Wiebcke, Y.-S. Li, J. Caro, *Chem. Mater.* **2011***, 23*, 2262-2269; e) C. Zhang, J. Yan, J. T. Ji, D. Du, Y. Sun, L. Liu, X. Zhang, Y. Liu, *J. Membr. Sci.* **2022,** *641*, 119915; f) R. Wei, X. Liu, Z. Zhou, C. Chen, Y. Yuan, Z. Li, X. Li, X. Dong, D. Lu, Y. Han, Z. Lai, *Sci. Adv.* **2022,** *8*, eabm6741.

[16] a) Y. Song, Y. Sun, D. Du, M. Zhang, Y. Liu, L. Liu, T. Ji, G. He, Y. Liu, *J. Membr. Sci.* **2021**, *634*, 119393; b) F. Zhang, X. Zou, X. Gao, S. Fan, F. Sun, H. Ren, G. Zhu, *Adv. Funct. Mater.* **2012**, *22*, 3583-3590; c) B. S. Ghanem, R. Swaidan, X. Ma, E. Litwiller, I. Pinnau, *Adv. Mater.* **2014**, *26*, 6696-6700; d) Q. Song, S. Jiang, T. Hasell, M. Liu, S. Sun, A. K. Cheetham, E. Sivaniah, A. I. Cooper, *Adv. Mater.* **2016**, *28*, 2629-2637.

[17] a) L. M. Robeson, *J. Membr. Sci.* **2008**, 320, 390-400; b) B. Belaissaoui, E. Lasseuguette, S. Janakiram, L. Deng, M.-C. Ferrari, *Membranes* **2020,** *10*, 367-390.

10.1002/anie.202216697



WILEY-VCH

## Entry for the Table of Contents

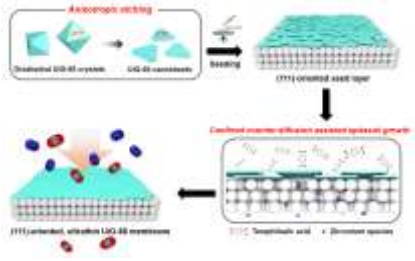

Highly oriented sub-200-nm-thick UiO-66 and $NH_2$-UiO-66 metal-organic framework membranes show unprecedented $CO_2/N_2$ and $H_2/CO_2$ separation performances, respectively. Their formation was aided by the preparation of uniform triangular-shaped UiO-66 nanosheet seeds via anisotropic etching, confined counter-diffusion-assisted epitaxial growth, and the use of a $ZrS_2$ source during epitaxial growth.